Generalized Three-Dimensional Imaging Algorithms for Synthetic Aperture Radar With Metamaterial Apertures-Based Antenna

ZHENHUA WU[1,2]**, LEI ZHANG**[3]**, AND HONGWEI LIU**[1,2]**, (Member, IEEE)**
[1]National Laboratory of Radar Signal Processing, Xidian University, Xi'an 710071, China
[2]Collaborative Innovation Center of Information Sensing and Understanding, Xidian University, Xi'an 710071, China
[3]School of Electronics and Communication Engineering, Sun Yat-sen University, Guangzhou 510275, China

Corresponding author: Lei Zhang (leizhang@xidian.edu.cn)

ABSTRACT Due to the flexibility in system design and small form factors, frequency-diverse imaging regime gained popularity in recent millimeter-wave (MMW) computational imaging (CI) research trends. In principle, frequency-diverse imaging systems produce the pseudorandom and spatially variant radiation fields to interrogate spatial information and reconstruct scene images using computational algorithms. Specifically, artificially structured metamaterials apertures antennas (MAA) have gained traction for their ability to manipulate electromagnetic waves in a deliberate and controlled manner. Combined with synthetic aperture radar (SAR) technologies, by moving a linear shape MAA in crosswise direction, fully three-dimensional (3D) scene images could be obtained through antenna motion. Focusing on the peculiar imaging geometry, we propose two kinds of postprocessing algorithms to black achieve 3D scene images reconstruction. The crux of the post-processing algorithms rely on the decoupling between cross-range dimension and antenna platform direction in the imaging domain, allowing the scene to be partitioned into a number of cross-range slices and reconstructed in a parallel manner. Compared with the traditional image reconstruction algorithms in frequency-diverse imaging, the proposed algorithms are more efficient and could effectively achieve 3D scene space observing. The extensive imaging simulations are conducted to verify the effectiveness of the proposed algorithms.

INDEX TERMS Computational imaging (CI), synthetic aperture radar (SAR), metamaterials apertures antenna (MAA), millimeter-wave imaging, decoupling.

I. INTRODUCTION

Active microwave and millimeter-wave (MMW) imaging techniques are superior to many other imaging techniques for providing non-ionizing radiation and have a variety of applications for security screening [1]–[3], medical diagnosis [4], non-destructive testing [5] and through-wall imaging [6], [7], etc. For conventional MMW imaging modalities, the spatial sampling of the physical aperture needs to satisfy the Nyquist sampling theorem to guarantee the diffraction-limited image reconstruction, generally inevitably resulting in a bulky and complex system hardware. In recent research trends, the modern computational imaging paradigms, including coded apertures [8], single-pixel imaging [9], and frequency-diverse imaging [10], have shown to be capable of offering possible solutions to the aforementioned problems. Particularly, a magnitude of holographic metasurface antennas with different architectures, such as metamaterial apertures [11]–[15], cavity apertures [16], [17] and metallic leaky cavity [18] have populated the CI imaging regime. These metasurface antennas are appealing as they can be easily fabricated using standard printed circuit board (PCB) techniques, leading to extremely low-costs and compact system form factors.

The associate editor coordinating the review of this manuscript and approving it for publication was Wanchen Yang.

Among these metasurfaces frequency-diverse imaging modalities, the waveguide-fed metamaterial apertures antennas (MAA) have received long-lasting attention since the first proof-of-concept imaging experiment was demonstrated by Hunt *et al.* [11]. In general, different from the classical metamaterial antennas [19], [20], these antennas consists of a rectangular waveguide loaded with a multitude of artificially structured metamaterials. As the driving frequency of the waveguide mode is swept, different subsets of these frequency-agile resonators couple a portion of the guided mode's energy to free space, producing a sequence of nonoverlapping and complex radiation fields. Using frequency diversity, a series of measurement modes can be obtained to encode scene information and preferentially enable computational imaging techniques to retrieve high-fidelity images. Subsequently, to satisfy the need for beam-forming and wave-front controlling capabilities in SAR imaging, the independent control to each resonator has been introduced in MAA, yielding the dynamic metamaterial apertures (DMA). In [21] a K-band DMA consisting of voltaged-controlled metamaterial apertures with diodes integrated is demonstrated to perform 2-D and 3-D SAR imaging. In [22] both stripmap mode and spotlight mode 2D SAR imaging are experimentally presented with a X-band DMA consisting of liquid-crystal-switched radiating elements. Later in [23] the GPU-accelerated 3-D SAR imaging experiments are demonstrated with a semiconductor-based DMA. For 2D and 3D SAR image reconstruction of frequency diverse antennas, there are mainly two kinds of post-processing algorithms. One common reconstruction approach is to directly solve the measurement equation corresponding to imaging scene using the straightforward matrix inversion technique [21]–[23]. Comparatively, in [24], [25], the range migration algorithm (RMA) has been adapted for the mask-based DMA to perform image reconstruction in both stationary and moving case, showing high computation efficiency against the matrix inversion approach.

In this paper, we focus on developing efficient 3D post-processing imaging algorithms for SAR with MAA, in which a linear shape MAA is physically moved in horizontal direction while forming random diverse pattern to gather information from the vertical direction. This peculiar SAR configuration is intrinsically similar to the system proposed by Sheen *et al.* [26], where the coherent one-dimensional electronically switched antenna array is replaced by a linear shape MAA. The crux of the post-processing algorithms lies in the decoupling of the synthetic aperture dimension and the MAA platform direction, acquiring cross-range information and range information respectively. Compared with the commonly used matrix inversion approach for SAR image reconstruction of frequency-diverse antennas [21]–[23], our algorithm is more efficient and able to effectively handle large scene data sets. Besides, different from the work in [21], [25], the specific locations of the imaged object (region of interest) in scene space are not artificially confined, both the pre-processing step and the induced prior information of object

location in scene space are avoided. Since multiple masks need to be switched at each spatial sampling position for DMA, we do not rigorously pursuing the DMA architecture to perform 3D imaging considering the extra time consumption. Herein, the appealing frequency-diversity peculiarity of MMA is our main concern, and we aim to provide a thorough and systematic approach for MAA to perform whole scene space observing.

The rest of this paper is organized as follows. In Section II, we will briefly introduce the generally applied forward imaging model in frequency-diverse imaging literature. Section III is devoted to the derivation of back-projection algorithm and the imaging simulation is given. Section IV is devoted the derivation of omega-K algorithm to achieve 3D scene images. Imaging simulations using a simulated one-dimensional MAA are given in Section V. Finally, conclusions are presented in Section VI.

II. FORWARD IMAGING MODEL

In this section, we will briefly introduce the system configuration and imaging principle of MAA. The MAA generally consists of a parallel-plate waveguide driven by a coaxial feed probe that launches a guided wave within the structure. In the actual fabricated MAA, the complementary electric inductive-capacitive (cELC) elements tailored with different physical geometries are integrated into the upper conductor of a microstrip transmission line. The injected microwave propagates over the aperture to excite multiple radiating elements simultaneously, resulting in a beam pattern with a large number of lobes, the specific turning mechanism and resonating character of cELC elements are exhaustively discussed in [27]. Consider a monostatic frequency-diverse metamaterial imaging system depicted in Fig. 1, where metamaterial apertures panel is used as transmitting antenna while an open ended waveguide (OEWG) probe is used as receiving antenna, comprising a panel-to-probe configuration. As the driving frequency changes, the radiation field excited from different subsets of resonators changes. Objects within the scene scatter the incident fields, producing the backscattered components detected by the waveguide probe at transmitting antenna plane. OWEG has large bandwidth and low gain, ensuring that an ample backscattered signal is collected from all possible directions and at all frequencies. In the following derivation, the vector $\vec{\mathbf{r}}$ indicates the points on the reference (MAA) plane, the vector $\vec{\mathbf{r}}'$ represents points in imaging scene.

To describe the imaging process discussed above, a commonly adopted inverse scattering model in frequency-diverse literature is the first Born approximation, where the perturbation of scatters to the interrogating field is assumed to be weak. The effectiveness and accuracy using the first Born approximation have been extensively confirmed through imaging experiments [11]–[15]. Applying this approximation, the frequency measurements collected by the receiving probe are related to the scene reflectivity through the measurement matrix (transfer function), which is the product
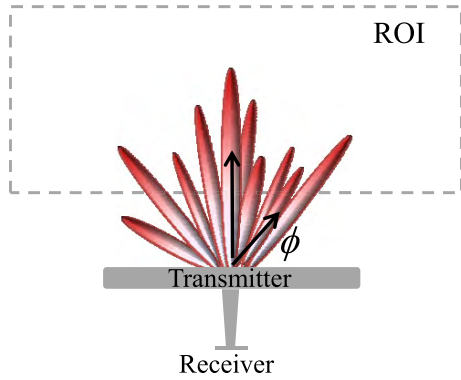
FIGURE 1. The definition of the region of interest and the panel-to-probe system layout.

of the electric fields from the transmitting aperture and the receiving probe at each location in the scene. The total fields that propagate into the OEWG have the following proportionality:

$$\mathbf{g}(f) \propto \int_V \mathbf{U_{0TX}}(\vec{\mathbf{r}}';f)\mathbf{U_{0RX}}(\vec{\mathbf{r}}';f)\sigma(\vec{\mathbf{r}}')\,\mathrm{d}^3\vec{\mathbf{r}}' \qquad (1)$$

where $\mathbf{U_{0TX}}(\vec{\mathbf{r}}')$ and $\mathbf{U_{0RX}}(\vec{\mathbf{r}}')$ denote the transmitted and received fields, respectively, σ represents the scene reflectivities. Since the system is both diffraction and bandwidth limited, (6) can be written as a general and concise matrix equation:

$$\mathbf{g} = \mathbf{H}\sigma + \mathbf{n} \qquad (2)$$

where $\mathbf{g} \in \mathbb{C}^{M \times 1}$ is the receiving measurement vector collected by the low-gain OWEG, and $\sigma \in \mathbb{C}^{N \times 1}$ denotes the unknown reflectivity vector of scene space, $\mathbf{n} \in \mathbb{C}^{M \times 1}$ is an additive noise term included for generality, and $\mathbf{H} \in \mathbb{C}^{M \times N}$ is the measurement matrix. Broadly speaking, within the first Born approximation, the above linear equation provides a clear and sufficient description of the process of emitting and coherently receiving electromagnetic wave scattered by scene object.

To reconstruct the scene information, the matrix equation described in (2) needs to be solved for σ. In theory, various matrix inversion algorithm have been proposed for both well and ill-conditioned $\mathbf{H}$. In the simplest implementation, assuming additive white Gaussian noise, a matched filter (MF) reconstruction suitably solves (2) as $\hat{\sigma}_{est} = \mathbf{H}^\dagger\mathbf{g}$, where $\dagger$ denotes the conjugate transpose operator. Given the easy implementation capability, the matched filter approach is commonly applied in current frequency-diverse imaging systems using arbitrary field patterns. Besides, more advanced reconstruction algorithm like least squares algorithm and regularization methods are also widely used. Note that when $\mathbf{H}$ is extremely underdetermined ($M \ll N$), the estimation with MF method of under-sampled scenes could be further refined with more sophisticated reconstruction algorithms. By imposing a ℓ_1-norm penalty, the estimation of σ could

be transformed as the following optimization problem

$$\tilde{\sigma} = \arg\min_{\sigma}\{\|\mathbf{y} - \mathbf{H}\sigma\|_2 + \lambda\|\sigma\|_1\} \qquad (3)$$

where λ is the regularization factor directly related to the noise level, $\|\cdot\|_2$ denotes the ℓ_2-norm, the first term in (3) implies the fidelity of data fitting (consistency), which is used to minimize the reconstruction error, and the latter corresponds to a regularized term reflecting the prior information that we would like to impose.

A. MEASUREMENT MATRIX CHARACTERIZATION
Note that the accurate reconstruction of scene reflectivities require the precise characterization of transmitting MMA fields and receiving probe fields, in most imaging experiments of the current frequency diverse imaging literature [12]–[18], [21], the imaged object region is often confined to a certain area (often Fresnel zone, at a range of 0.5~1m). In such imaging scenarios, the near-field response of the transmitting MAA, denoted by $\mathbf{\Phi}$, can be experimentally measured through near-field scanning in the laboratory environment, and the transmitted fields $\mathbf{U_{0TX}}(\vec{\mathbf{r}}')$ corresponding to arbitrary location in scene space are calculated with the near-field response as well as the plane-to-plane propagator. The propagation model between arbitrary positions $\vec{\mathbf{r}}'_a$ and $\vec{\mathbf{r}}'_b$ can be represented by free space Green's function

$$\mathbf{G}(K, \vec{\mathbf{r}}'_a, \vec{\mathbf{r}}'_b) = \frac{e^{-jK|\vec{\mathbf{r}}'_a - \vec{\mathbf{r}}'_b|}}{4\pi|\vec{\mathbf{r}}'_a - \vec{\mathbf{r}}'_b|} \qquad (4)$$

where, K denotes the wavenumber, $\mathbf{G}$ has a number of rows equal to the number effective sources and a number of columns equal to the number of scene locations. The transmitted fields $\mathbf{U_{0TX}}(\vec{\mathbf{r}}')$ can be written as: $\mathbf{U_{0TX}}(\vec{\mathbf{r}}') = \mathbf{\Phi}\mathbf{G}$. In our demonstration, to provide wide scene space observing, we assuming scenes are illuminated by far-field radiation from MAA, and the imaging scenario is similar to the demonstrations by Hunt et al. [11]. In this case, the radiation fields in arbitrary scene space are computed with the far-field pattern of MAA, denoted by T and the linear propagation phase term e^{-jKR}, $\mathbf{U_{0TX}}(\vec{\mathbf{r}}')$ can be expressed as: $\mathbf{U_{0TX}}(\vec{\mathbf{r}}') = Te^{-jKR}$, the detailed far-field characterization method of MAA can be found in [28]. The received fields of OEWG probe is calculated with the far field pattern, denoted by Ψ, in conjunction with the linear propagation phase e^{-jKR}, $\mathbf{U_{0RX}}(\vec{\mathbf{r}}')$ can be computed with: $\mathbf{U_{0RX}}(\vec{\mathbf{r}}') = \Psi e^{-jKR}$.

In this section, the scene images reconstruction methods for static MAA are presented, and the imaging scenario as well as the measurematrix characterization method used in our demonstration are specified. 3D SAR imaging postprocessing algorithms are given in the subsequent sections.

III. SAR IMAGING WITH MAA
With the aim of acquiring high resolution observing for spaceborne and airborne radar systems, tremendous progress has been made in the synthetic aperture radar technology over

the past decades, until now, it remains to be a research hotspot in radar imaging literature. Specifically, an antenna with a directive beam is mounted on a moving platform that traveled along a long distance, electromagnetic waves are sequentially transmitted and the backscattered echoes are coherently collected in multiple observing points. Through sophisticated post-processing algorithms, the synthesized beamwidth is much narrower than the physical antenna beamwidth, yielding dramatically increased resolution images without the hardware burden of a large physical aperture antenna. Depending on the observation needs, multiple SAR imaging modalities have been developed to acquire either two-dimensional (2D) or three-dimensional (3D) scene images, among which stripmap SAR and spotlight SAR are two wildly used modes. In stripmap mode, the antenna beam orientation is held constant with respect to the airborne flight path when the antenna aperture travels, illuminating a swath of a scene. While in spotlight mode, to focus on illuminating a particular region of imaging scene, the beam is continuously steered as the airborne platform flies. Note that to generate highly directive beam, the gimbal-actuated (reflector dishes and horn antennas) and phased-arrays antennas are commonly utilized in traditional SAR imaging radars. Given the radiation efficiency and favorable frequency-diverse field patterns of MAA, both stripmap spotlight SAR near range 2D imaging experiments have been extensively demonstrated in recent research [21]–[23], showing appealing advantages compared to conventional antennas.

In this paper, we focus on investigating 3-D MAA imaging where the antenna aperture is translated along a path perpendicular to its length. Compared to the system configuration presented by Sheen *et al.* [26], MAA utilize spatially diverse field pattern instead of multistatic antenna array to sample the spatial frequency components (k-components), we believe the low profile and lightweight form factor merits of MAA can be taken full advantage in this imaging scenario. We start by demonstrating the 3D SAR imaging configuration of MAA, pointing out that the key postprocessing technique relies in the decoupling between the antenna movement direction and the length direction. Next, to achieve full volumetric imaging, a series of classical SAR imaging algorithms are adapted to conduct 3D imaging simulations.

To create 3D images, a MAA platform needs to move in a crosswise path that is perpendicular to its length, as shown in Fig. 2, where a bistatic SAR configuration is depicted. The direction parallel to the direction of the antenna platform motion is cross-range, and the directions orthogonal to the direction of antenna platform motion are the ground range and elevation. In this scenario, the spectral bandwidth provides range resolution and the MAA aperture provides spatial diversity for vertical resolution, by translating the MAA along the z-direction, additional information can be obtained to achieve cross-range resolution. The Cartesian coordinate system O-xyz is established, the origin is located at the center of the scanning path, x-, y-, z-axes denote the ground-range, azimuth, and height directions, respectively. At each
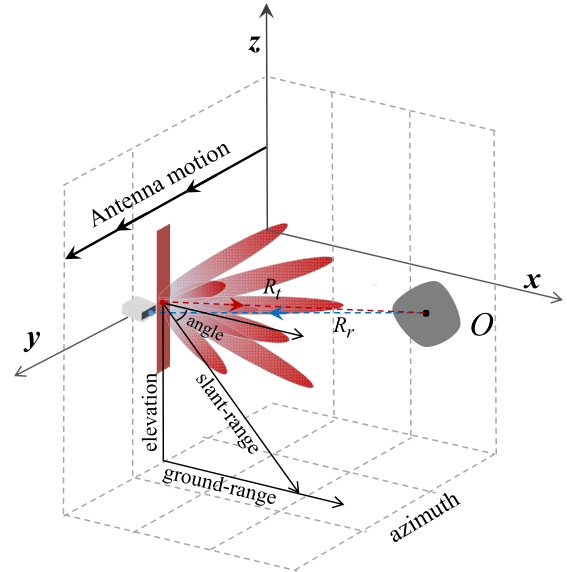
FIGURE 2. Illustration of the 3-D SAR imaging system using a MAA, the antenna moves in a crosswise path that is perpendicular to its length configuration.

scanning position, the MAA transmits a band-limited signal that illuminates the scene within the field of view (FOV). The location of the transmitting MAA is $(0, y_t, 0)$, and the location of receiving probe is $(0, y_r, 0)$, O represents an arbitrary point on the target with coordinate (x, y, z) and reflectivity $\sigma(x, y, z)$. The receiving probe changes in accordance with the transmitting MAA simultaneously.

Then the respective distances from the transmitting MAA center and receiving probe to the position O are given by

$$R_t = \sqrt{x^2 + (y - y_t)^2 + z^2} \qquad (5)$$

$$R_r = \sqrt{x^2 + (y - y_r)^2 + z^2} \qquad (6)$$

As discussed in [29], the measurement matrix takes the form of transmitting fields and receiving fields, hence **H** can be written as:

$$\mathbf{H} = \mathbf{U_{0TX}}(\vec{r}'; f)\mathbf{U_{0RX}}(\vec{r}'; f) = Te^{-jKR_t} \cdot \Psi e^{-jKR_r} \qquad (7)$$

Throughout this paper, K is the free space wavenumber, $\sigma(x, y, z)$ is reflectivity of the object. In practical, the targets range significantly larger than the transmitting and receiving antenna spacing, though the transmitting MAA and the receiving probe may not share the same phase center, with the paraxial approximation (the antenna spacing with respect to the wavelength), we treat the imaging geometry as a quasi-monostatic configuration, that is $R_t = R_r$. In this consideration, the measured signals of receiving probe at different spatial location are

$$S(R_t, K) = \iiint T \cdot \Psi \cdot \sigma(x, y, z)e^{-j2K\sqrt{x^2 + (y - y_t)^2 + z^2}}$$
$$dxdydz \qquad (8)$$

Note that the observed scene space would increase rapidly with the antenna's movement, which inevitably yield the multiplicative scaling of the dimensionality of the measurement matrix. In practical, the measurement matrix with extremely large scale pose significant challenge in both memory storage and imaging computation costs. It is therefore necessary to utilize other imaging post-processing techniques to deal with the massive computation costs brought with the large data sets. In the following imaging simulations, point scatterers are located in 3D scene space and illuminated by the synthetic aperture MAA, and toward the goal of decoupling between the crosswise direction and lengthwise direction in imaging domain, two representative processing algorithms in classical SAR imaging literature are examined.

IV. BACK PROJECTION ALGORITHM

Since the invention of SAR techniques in the late 70s, many image formation algorithms have been developed. The majority of the those methods in practice mainly contain two kinds: time-domain algorithms and frequency domain algorithms. Frequency domain methods perform calculations with respect to the frequency of a signal rather than the timing of the signal. In general, frequency domain algorithms are computationally efficient as the major calculations are implemented with fast Fourier Transforms (FFT). Nevertheless, there has not been a generalized algorithm suitable for all types of imaging scenarios (e.g., low squint, spotlight mode geometry, narrow range swath, etc), that is, these algorithms may need to be modified in order to suit a particular situation. On the contrary, the time-domain backprojection (BP) algorithm doesn't suffer from these limitations, the same algorithm may be applied to all imaging geometries, the major downside to time-domain BP algorithm is that it is more computationally expensive, making it unacceptable in many real-time imaging scenarios. Because of this, many efforts have been devoted to enhance the efficiency of BP algorithm, the detailed researches can be found in [30], [31].

Towards the goal of forming the target reflectivity function $\sigma(x, y, z)$ at a given grid point (x, y, z) in the spatial domain, BPA provides high imaging precision by coherently accumulating the received signal that corresponds to all synthetic aperture locations. Following this idea, to reconstruct the spatial distribution of the reflectivity $\sigma(x, y, z)$ using the collected data $S(R_t, f)$, one can write the inversion form of (8):

$$\sigma(x, y, z) = \int_{y_t} \int_f T^{-1} \Psi^{-1} \cdot S(R_t, f) e^{j2K\sqrt{x^2 + (y-y_t)^2 + z^2}}$$
$$dy_t df \quad (9)$$

It should be clarified that the radiation field pattern T considered here is both frequency and angular modulated, it is a varying function of frequency as well as the target and antenna coordinates. And the radar target reflectivity function $\sigma(x, y, z)$ is assumed to be frequency and aspect angle independent over the frequency band and angular sector of interest. To achieve the angular resolving in the antenna movement
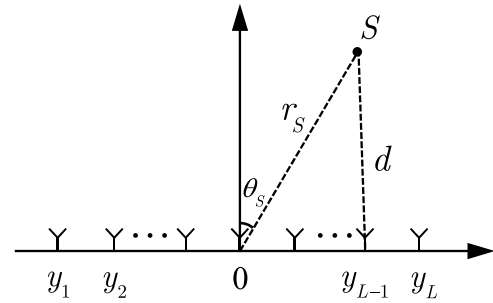

FIGURE 3. Near range source receiving geometry of virtual uniform linear array.

direction, the received data are backprojected over the spatial angular gird. As noted by Jakowatz *et al.* [32], [33], the fundamental concept of delay-and-sum beamforming (BF) that employs signal data collected by a multi-element array is inherently rooted in BPA. That is, to separate the signal arriving from a given direction, one can apply a set of linear phase delays to the array elements to cancel the linear phases that are inherently imposed on the arriving signal. Considering the vertical imaging resolution depends on the angular resolution of MAA, to realize the full potential of MAA, the imaged objects lie in a near range in our demonstration and we use the near range BF techniques to achieve angular resolving. Fig. 3 demonstrates the receiving geometry of uniform linear array in near-range consideration, and each virtual element y_l represents a spatial sampling location of MAA.

We use the above virtual array geometry to deduce the near-range steering vector to achieving beam-forming procedure. An array of horizontal antenna elements are positioned linearly along the y-axis with coordinates of $y_1, y_2, \ldots y_L$ and the coordinates of source signal S with respect to the reference element are (r_s, θ_s). Taking the middle element m_0 as the origin, the distance between the source signal S and the m-*th* element can be computed using the law of cosines:

$$d_{m_0, s}(r_s, \theta_s) = \sqrt{y_{m_0}^2 + r_s^2 - 2y_{m_0} r_s \sin \theta_s} = r_s \quad (10)$$

$$d_{m, s}(r_s, \theta_s) = \sqrt{y_m^2 + r_s^2 - 2y_m r_s \sin \theta_s} \quad (11)$$

The set of linear phases that steer the array to the given direction θ_S, termed array vector in array antenna theory, can be written as:

$$\varphi(r_s, \theta_s) = \begin{bmatrix} \frac{r_s}{d_{1,s}(r_s,\theta_s)} \exp\{-jK[d_{1,s}(r_s, \theta_s) - r_s]\} \\ \frac{r_s}{d_{2,s}(r_s,\theta_s)} \exp\{-jK[d_{2,s}(r_s, \theta_s) - r_s]\} \\ \vdots \\ 1 \\ \vdots \\ \frac{r_s}{d_{M,s}(r_s,\theta_s)} \exp\{-jK[d_{M,s}(r_s, \theta_s) - r_s]\} \end{bmatrix} \quad (12)$$

where L is the number of the array elements. For the goal of achieving angular resolving in the crosswise direction, the bearing angles θ_s are steered sequentially, and the applied
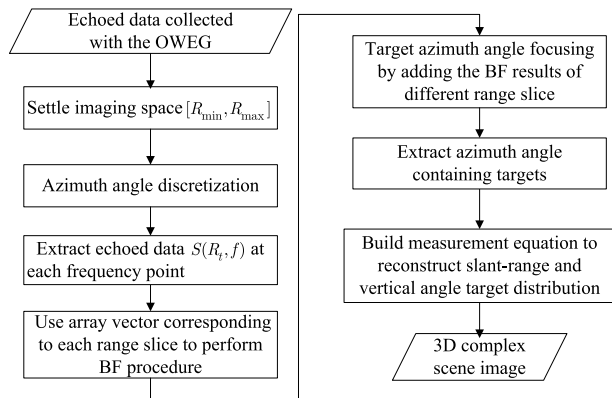
FIGURE 4. Block diagram of the near range backprojection algorithm applied for 3D SAR imaging with MAA.

Operation bandwidth	18.5~25 GHz
Antenna panel size	40 cm
Frequency sampling interval	8.125 MHz
Field of view (Azimuth)	$-45° \sim 45°$
Azimuth sampling interval	1.5°
Dimensions of T	801×48

linear phase sequence $\varphi(r_s, \theta_s)$ are then added with the collected data $S(R_t, f)$. This delay-and-sum beamforming concept is rooted in the principle of BP integral algorithm in (9).

To reconstruct the spatial distribution of the reflectivity σ, we use the cross-range angular filter (array vector) $\varphi(r_s, \theta_s)$ to match the reflected data $S(R_t, f)$ collected by OWEG at a series of spatial sampling points. However, due to the inherent curvature of the wavefront in near-range imaging space, the consistency of the array vector φ in the far-field application no longer hold and needed to be calculated respectively for each slant range slice R. The total angular response is the superposition of BF results that corresponds to target in the same bearing angle but different distances. Besides, it should be emphasized that given the wideband operation and the frequency varying feature of the radiation field pattern T, the array vector needs to be calculated at each corresponding frequency point (measurement mode). At each operation frequency point, BF procedure is performed across the entire virtual array, and the bearing angle is discretized according to a prespecified angular grid. After BF procedure, targets in imaging space can be well resolved in different azimuth angular sectors, and the echoed signals collected at cross-range dimension are transformed into different cross-range azimuth angulars, we then extract the azimuth data that contains targets to perform two-dimensional (slant range and vertical angles) reflectivities reconstruction. We can summarize the flowchart of back-projection algorithm using BF techniques in Fig. 4.

A. NUMERICAL SIMULATIONS

To focus on the implementation of the proposed algorithm, it should be clarified that a noiseless scenario is considered throughout the subsequent imaging simulations. We now consider reconstructing the complex reflectivity of several ideal point scatterers located in the imaging grid using the simulated echoed data.

The employed measured radiation field pattern of MAA[1] are from [11], and the antenna parameters are given in Table 1. The prototype consists of a 1D leaky waveguide, formed by patterning the top conductor of a standard microstrip line with resonators, and is capable of imaging of 2D (azimuth angle plus range) canonically sparse scenes. MAA is vertically placed parallel to the z-axis, the spatial sampling interval in y-axes is 0.005 with a range of [-1.5,1.5]m. At each location, wide frequency band signals are transmitted and received by the OWEG. As depicted in Fig. 5(a), five scatterers are located in the imaging scene ranging from [2.8,3.8]m with azimuth coordinates are -1, 0, 1m, respectively, and the magnitude of each scatterer obeys to $\mathcal{CN}(0, 1)$.

Fig. 5 shows the 3D MAA imaging results using BP integral algorithm, the azimuth region is divided with a fixed interval of 0.9° among $[-45°, 45°]$. Fig. 5(b) is the BP result corresponding to the target at the slant range of 3m, we can see that the point scatter at a slant range of 3m are well focused and resolved in azimuth angular space. By contrast, targets at the range of 3.2m are defocused due to mismatch of the array vector. The result in Fig. 5(c) is quite opposite to Fig. 5(b) since the array vector is corresponding to the 3.2m slant range slice. We then perform the BP across the whole imaging space across the slant range dimension, all results are added together, yielding the target azimuth angle focusing result. From Fig. 5(d), we can clearly observe that all scatterers in the imaging domain are preferably separated in different azimuth angles. Note that, during the point-wise BP implementation, the target response with a well-focused angle and slant range can be clearly observed, as the propagation delay phases in different receiving locations have been well compensated, we can then directly build the measurement equation using $T\cdot$ and extract the azimuth focused data to directly reconstruct the slant-range and vertical angle reflectivities distribution. The elevation angle and slang-range spatial distribution of reconstructed scatterers corresponding to three azimuth angulars are shown in Fig. 5(e)-(g), respectively, the spatial coordinates of scatterers can all be clearly observed.

For the goal of decoupling between azimuth and lengthwise direction in imaging domain, an azimuth beamforming procedure is firstly adopted to achieve angular resolution, each angular resolution sector that contains targets can be further reconstructed using the inherent operator radiation fields

---

[1]Available at Web site: http://science.sciencemag.org/content/339/6117/310/tab-figures-data

(a)

(b)

(c)

(d)

(e)

(f)

(g)
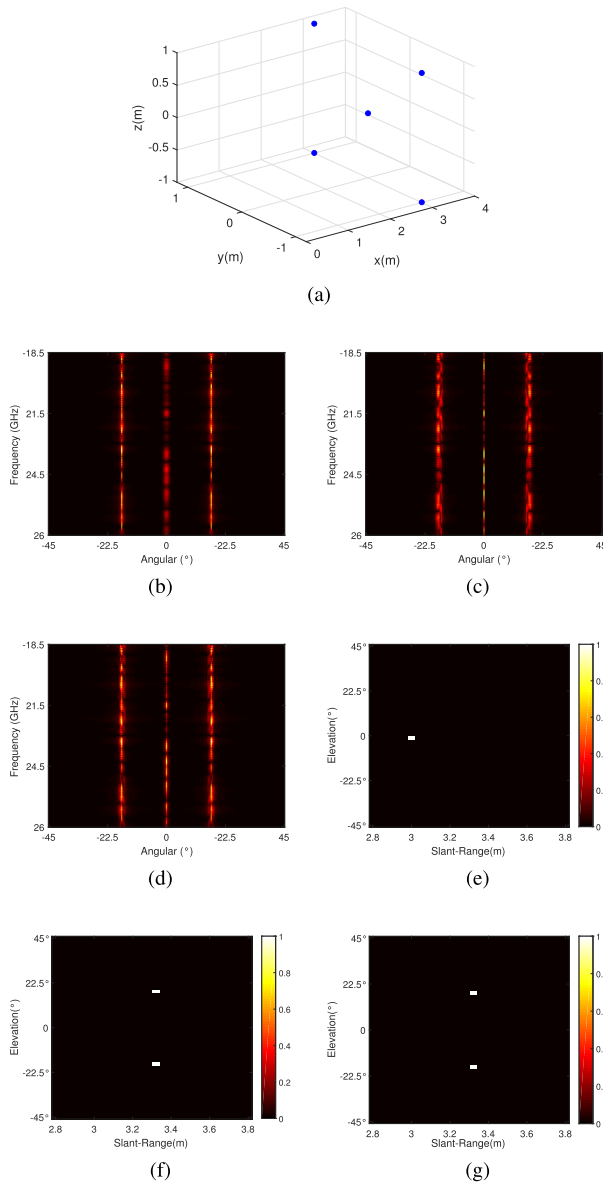
FIGURE 5. 3D scene imaging using BPA. (a) Spatial distribution of the point scatterers. (b) BP results with respect to the slant range of 3m. (c) BP results with respect to the slant-range of 3.2m. (d) Overall BP results. (e) Elevation and slant-range reconstruction corresponding to azimuth angle of −18°. (f) Elevation and slant-range reconstruction corresponding to azimuth angle of 0°. (g) Elevation and slant range reconstruction corresponding to azimuth angle of 18°.

pattern T. Whereas, due to the inherent wavefront curvature in near range imaging, BF procedure needs to be performed pointwise in scene space across the entire operation frequency spectrum, which leads to a degraded computation efficiency to a certain extent. We then examine the classical omega-K algorithm in this particular 3D SAR imaging simulation in the subsequent section.

V. OMEGA-K ALGORITHM

Omega-K algorithm has been a popular postprocessing algorithm in frequency domain algorithms for the advantage

of fast implementation and involving no approximation in range cell migration (RCM)-the inherent wavefront curvature caused by the antenna movement. Generally, omega-K performs image reconstruction in the frequency-wavenumber domain, since the frequency and spatial wavenumber along the range direction are connected through the free space dispersion relation, with Stolt interpolation, the coupling terms between slant range and azimuth wavenumbers in wavenumber domain can be removed, enabling fast Fourier transforms (FFTs) to be applied. This approach of resampling data from the frequency domain to the wavenumber domain forms the basis for the range migration algorithms (RMA) commonly used in SAR imaging. In the following, we will demonstrate the ability of omega-K algorithm in 3D SAR imaging using MAA.

Reviewing (8), by perform FFT across the coordinates y_r, the measured signal in the wavenumber domain takes the form of

$$S(K_r, K_y) = \int_y T \cdot \Psi \cdot \sigma(x, y, z) \frac{\exp(-j\pi/4)}{\sqrt{K_r^2 - K_y^2}}$$
$$\times \exp\{-j\sqrt{x^2 + z^2}\sqrt{K_r^2 - K_y^2} - jyK_y\}dy \quad (13)$$

where K_r represent the range wavenumber $K_r = \frac{4\pi f}{c}$, K_y is the azimuth wavenumber. In above equation, the amplitude term $\frac{\exp(-j\pi/4)}{\sqrt{K_r^2 - K_y^2}}$ is essential to accurately reconstruct σ and has been added for completeness. In the phase term, the latter corresponding to the azimuth position of the target, the range and azimuth wavenumbers are coupled in former phase term, and it is a function of target's slant range representing the spatial variance of RCM. According to the plane waves dispersion relation in free space:

$$K_r^2 = K_x^2 + K_y^2 + K_z^2 \quad (14)$$

By applying the variable replacement to $\sqrt{K_r^2 - K_y^2}$ with K_u, we have:

$$K_u^2 = K_r^2 - K_y^2 = K_x^2 + K_z^2 \quad (15)$$

Substituting (15) into (13), we obtain

$$S(K_u, K_y) = \int_y T \cdot \Psi \cdot \sigma(x, y, z) \frac{\exp(-j\pi/4)}{K_u}$$
$$\times \exp\{-j\sqrt{x^2 + z^2}K_u - jyK_y\}dy \quad (16)$$

The signal is thus transformed into the wavenumber domain assigned to K_u and K_y, and is distributed over an irregular grid of wavenumber values. Using Stolt interpolation, the wavenumbers in K_u domain are evenly sampled onto a uniform grid, ensuring the wavefront curvature is completely corrected and the wavenumber dataset is regularly mapped. To achieve the goal of resolving the target in spatial azimuth domain, an n-dimensional inverse Fast Fourier Transform (iFFT) needed be performed on the $S(K_u, K_y)$, the spatial
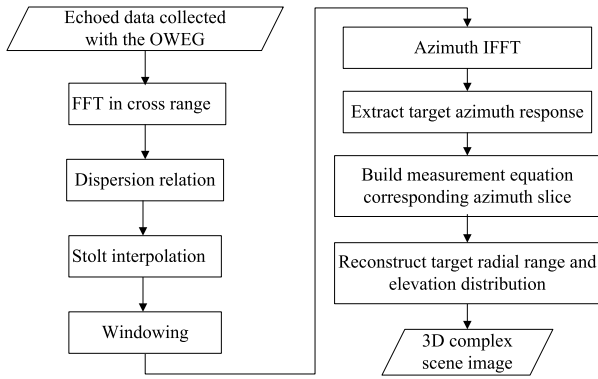
FIGURE 6. Block diagram of omega-k algorithm applied for 3D SAR imaging with MAA.

(a)

(b)

(c)

(d)

(e)

(f)

(g)

(h)

FIGURE 7. 3D scene imaging results using omega-k algorithm. (a) Received signal $S(K, y_r)$. (b) Result of the azimuth FFT. (c) K_u, K_y wavenumber distribution after Stolt interpolation. (d) Result iFFT with respect to K_y. (e) Section plane of the azimuth focusing results in (d), $K_u/K = 0.5$. (f) Azimuth focusing result for traditional SAR using OWEG. (g) Windowed iFFT with respect to K_y. (h) Section plane of the windowed azimuth focusing results in (g), $K_u/K = 0.5$.

iFFT of the wavenumber domain $S(K_u, K_y)$ with respect to azimuth wavenumber K_y can be written as :

$$
\begin{aligned}
S(K_u, y) &= \int_{K_y} S(K_u, K_y)\exp\{jyK_y\}dK_y \\
&= \int_{K_y} T \cdot \Psi \cdot \sigma(x, y, z) \frac{\exp(-j\pi/4)}{K_u} \\
&\quad \times \exp\{-j\sqrt{x^2 + z^2}K_u\}dK_y
\end{aligned} \tag{17}
$$

With the above discussion, target being imaged have been well resolved in azimuth dimension, each azimuth position $S(K_u, y)$ that contains targets can further be extracted to reconstruct the radial distance and elevation spatial distribution based on (17), the flowchart of omega-K algorithm is illustrated in Fig. 6.

A. NUMERICAL IMPLEMENTATION

In this subsection, numerical implementation of the omega-K algorithm was implemented. An *n*-dimensional FFT is performed on the received signal, and *n* depends on the specific spatial sampling points in *y*-axes. The azimuth wavenumber K_y is assigned according to the *y*-coordinates of the receivers, denoted by

$$
K_y = [-\frac{\pi}{y_{\min}}, \frac{\pi}{y_{\max}}] \tag{18}
$$

With the receiver sampling position in y-axis settled, K_y can be directly calculated, K_u can then be computed and evenly interpolated using Stolt mapping, the data in wavenumber domain is now distributed over an regular grid of K_u and K_y. In order to reconstruct the final image, we then perform IFFT with respect to K_y, achieving targets azimuth focusing in y-axis, that is, resolving the targets in spatial y-axis. Each azimuth resolution cell containing targets could be observed and the azimuth focusing data are extracted to perform CI imaging to reconstruct the spatial distribution in radial distance and elevation angle. Imaging simulations are shown in Fig. 7 and 8, all the system parameters are the same as the parameters in imaging simulations above.
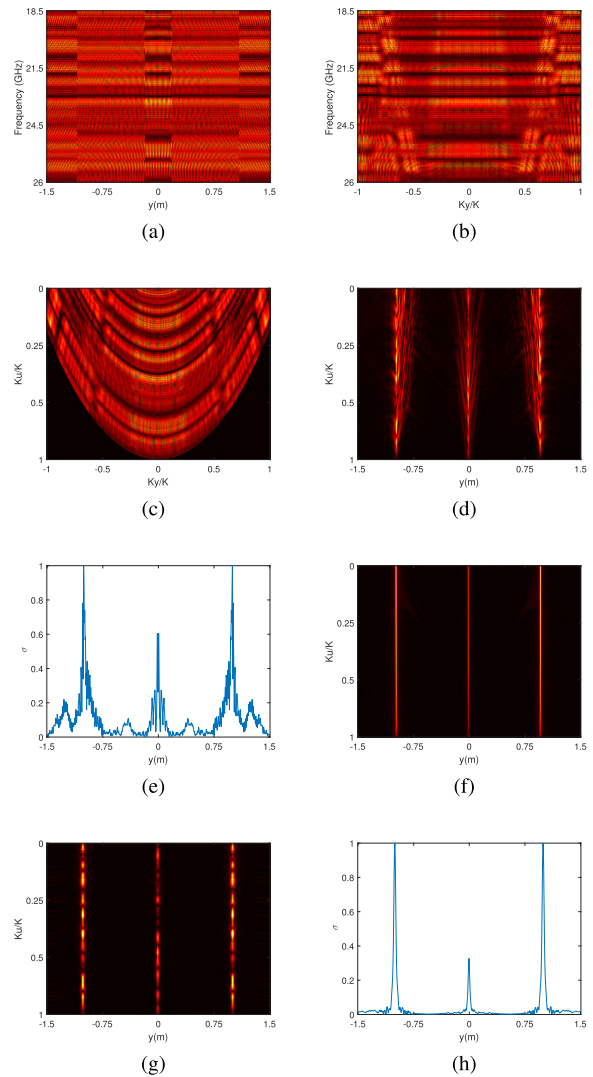
Fig. 7 show wavenumber coverage and azimuth focusing results. Fig. 7(b) is the simulated data in wavenumber domain, Fig. 7(c) is the wavenumber distribution after Stolt mapping and the azimuth *y* focusing result is shown in Fig. 7(d). In this figure, it is of particular interest to see that the spread function of targets in cross-range domain slightly differs from the traditional sinc-like function, in other words, the target responses are not perfectly focused in cross-range (see Fig. 7(e)). To find the reason for this evident difference, a comparison simulation is performed where the frequency-diverse radiation field pattern *T* is neglected and the system is in a traditional monostatic transceiver configuration. The azimuth focusing result is shown in Fig. 7(f). Compared with Fig. 7(d) and (f), we can deduce that the
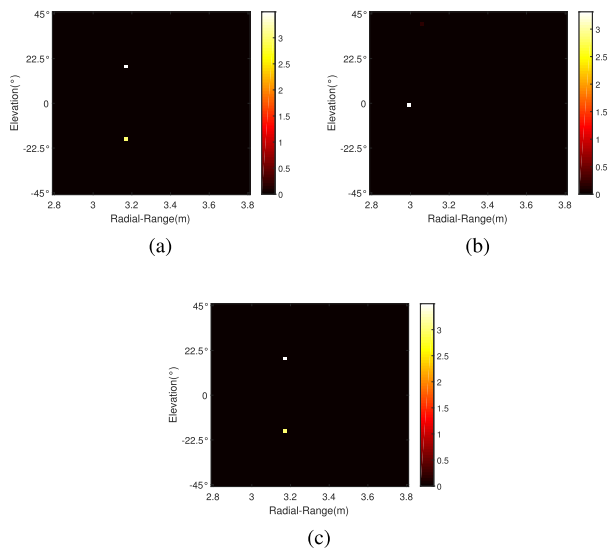
FIGURE 8. Radial range and elevation angle reconstruction. (a) Target distribution in radial range (x) and elevation (z) at *y* = −1m. (b) Target distribution in radial range (x) and elevation (z) at *y* = 0m. (c) Target distribution in radial range (x) and elevation (z) at *y* = 1m.

FIGURE 9. Simulated metamaterial apertures antenna configuration. (a) Edge feeds layout. (b) 3D radiation beam pattern at the central frequency of 35GHz.

existence of frequency modulating with respect to the range wavenumber Kr, would inevitably introduce perturbation in Stolt mapping procedure, yielding the incomplete focused target azimuth response function. In this consideration, the windowing implementation needed to be perform to suppress the sidelobe in azimuth focusing process. Fig. 7(g)and(h) are the azimuth focusing results after windowing manipulation, we can see that the scatterers are well focused in spatial azimuth domain.

The azimuth data containing scatterers are then extracted to perform 2D (radial-range plus elevation) image reconstruction. We treat the azimuth focusing data corresponding to $y = -1, 0, 1$ in Fig. 8(g) as the new measurement vector, each measurement matrix is then built based on a imaging space of [2.8, 3.8]m. The range resolution is calculated according to c/2B = 0.0214m, yielding the measurement matrix with dimensions of $801 \times (48 \times 44)$. Given the underdetermined ratio of the measurement equation, we adopt the classical sparse Bayesian learning (SBL) algorithm [34] to precisely reconstruct the 2D radial-range and elevation angle spatial distribution. The reconstruction results are shown in Fig. 9, where we can clearly observe that all scatterers are precisely preserved in this noiseless imaging simulation.

Compared with the two algorithms discussed above, BP integral algorithm need a prior information of the approximate range of the ROI, and scene space needs to be back-projected and accumulated in a pointwise fashion due to the inevitably wavefront curvature in near range imaging, yielding a relatively low computation efficiency. As for the omega-k algorithm, the calculation in wavenumber domain with FFTs is more efficient and the ROI prior information is not necessary. For qualitative comparison of computation costs, the main difference between these two algorithms
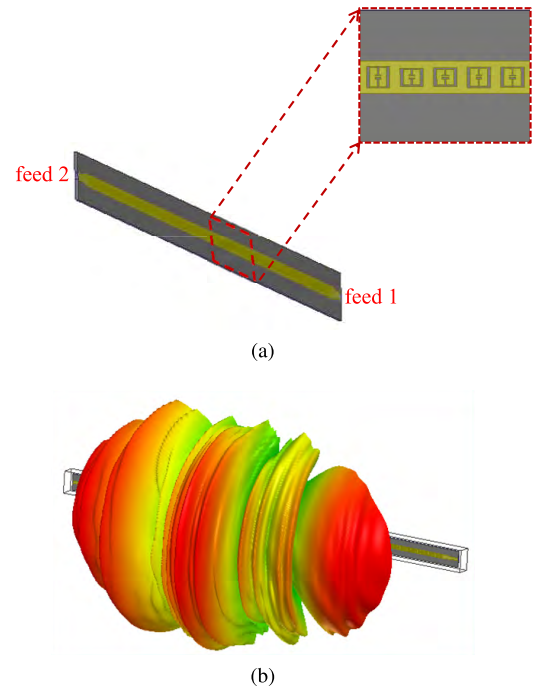
consists in the decoupling step. In BP integral algorithm, the near range beamforming procedure require point-wise calculation in all frequency modes, azimuth angles, and different range slices, hence the number of operations is $\mathcal{O}(N^3)$, N is the number of frequency modes, while in omega-k algorithm, the decoupling step using FFT requires a quite small number of operations $\mathcal{O}(N_a \log N_a)$, N_a is the number of aperture spatial sampling positions. Hence, we can say that omega-K algorithm is more efficient that BP integral algorithm. In addition, BP integral algorithm discretize scene space into different azimuth angular sectors, while in omega-k algorithm, the scene space is partitioned into Cartesian coordinates, the imaging results are more straightforward to follow.

VI. 3D IMAGING SCENE

In a similar fashion to the algorithm deduction described above, we demonstrate the aperture's ability to image 3D scenes using a combination of mechanical motion and frequency-swept measurements in this section. A one dimensional MAA is designed to perform fully 3D (range, azimuth and elevation) scene reconstruction. Imaging simulations are carried out based on the simulated radiation fields and imaging scenarios.

A. CONSTRUCTION OF THE ANTENNA

The metamaterial apertures used in this simulation are comprised of the complementary electric-inductive-capacitive (cELC)s, etched within the upper conductor of a microstrip waveguide. In our practical implementation, the physical structure of cELC element we adopt is originally designed

TABLE 2. System parameters of 2D metamaterial apertures antenna.

Operation bandwidth	31.5∼38.5 GHz
Antenna panel size	40 cm
Number of resonators	100
Frequency sampling interval	25 MHz
Field of view (Azimuth)	$-70° \sim 70°$
Azimuth sampling interval	0.7°
Dimensions of T	281×201

FIGURE 10. Fields radiating from the aperture illuminate 9 ideal point scatterers.

by Lipworth *et al.* in [14], and the geometries of cELC elements are engineered to achieve resonance frequencies within the operation band from 31.5 to 38.5GHz using Ansoft HFSS 15.0. In total, there are 100 elements, spaced 4mm apart, forming a 40cm aperture panel, and the thick substrate between the copper ground plane and conducting copper is 0.5mm. The metasurface is excited from two end launch feeds, as shown in Fig. 9(a). The well-designed resonators are etched into the upper conducting plane of waveguide with a random spatial distribution of resonance frequencies. The connector injects a cylindrical transverse electric-magnetic (TEM) mode that propagates away from the feeding point and couples to the metamaterial elements. The total full-wave simulation time is about eight hours using Ansoft HFSS 15.0 on a computer with Intel i7 CPU, 128 GB RAM and Nvidia Tesla K80. We illustrate the antenna configuration in Fig. 9, where the feeds layout of antenna panel and the simulated 3D radiation beam pattern at the driving frequency of 35GHz are shown.

B. IMAGE RECONSTRUCTION

The simulations are conducted in a panel-to-probe configuration, as depicted in Fig. 2, where the metamaterial apertures antenna is used to illuminate the scene and the low-gain probe collect the scattered signal. The imaging scenes are illuminated by far-field radiation from the antenna panel using 281 frequency sampling points, resulting in $\Delta f = 25$MHz across the operation frequency band, and the MUR is found to be MUR= $c/\Delta f = 12$m. The 7GHz frequency bandwidth sets the range resolution $\delta_r = 2.14$cm, and the expected azimuth angular resolution at the center frequency $f_c = 35$GHz are

$$\Delta\varphi_{az} = \frac{\lambda_c}{A} = 1.23° \tag{19}$$

Here, the radiation fields are sampled uniformly in azimuth at $\Delta\varphi_{az} = 0.7°$ within the field of view (FOV) of $\pm70°$. We can summarize the system parameters of the 1D MAA in Table 2.

In this section, a target consists of nine ideal point scatterers is placed in the imaging scene, as depicted in Fig. 10, the ground range coordinates of scatterers are 1.6, 1.8, 2m, and the azimuth coordinates are $-0.25, 0, 0.25$m, the elevation coordinates are $-1, 0, 1$m, respectively. Similarly, the magnitude of each scatterer obeys to $\mathcal{CN}(0, 1)$. Consistent with the quasi-monostatic layout in the previous section, a
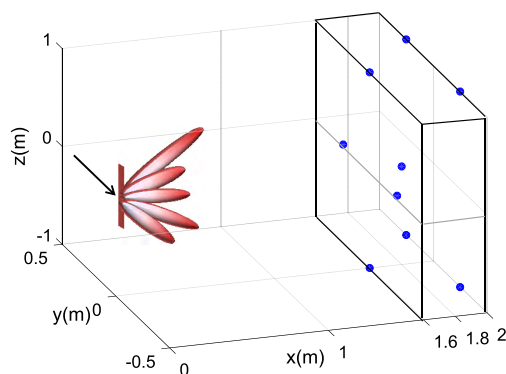
40-cm-long MAA operates as a transmitter, while a single OWEG situated next to the center of the MAA acts as a receiver, the system translates along the *y*-axis direction. The synthetic aperture is 3m long and is sampled at $\Delta_y = 5$mm.

According to (8), the receiving frequency measurements $S(R_t, K)$ is computed by multiplying the measurement matrix and the scattering coefficients. Note that the initial radiation field pattern is oversampled and need to be interpolated onto a regular grid according to the angular resolution. In real implementation, the antenna FOV is $(-45°, 45°)$, and angular sampling interval is $1.25°$, yielding the radiation field with dimensions of 281×73. In previous work demonstrated by Hunt *et al.* [13], the Gram matrix, denoted by $\mathbf{G} = T^{\dagger}T$ and $(\cdot)^{\dagger}$ is the complex conjugate transpose operator, is shown to be a suitable metric to characterize the radiation field pattern. The more closer approximation to the identity matrix, the better reconstruction performance is guaranteed. Considering the efficiency of proposed algorithm, 3D imaging scene is reconstructed using omega-K algorithm in this simulation, imaging results are given in Fig. 11. Fig. 11(a) is the magnitude distribution of the simulated radiation field pattern T, Fig. 11(b) shows the magnitude of the corresponding Gram matrix, demonstrating its close approximation to the identity matrix. Fig. 11(c) is the transformed signal in the wavenumber domain, Fig. 11(d) is the azimuth focusing result with window manipulation, we can see that scatterers are preferably resolved in cross range *y* coordinate, whereas, due to the natural frequency-modulated characteristic of radiation field T, the target azimuth response slightly differs from the traditional sinc-like function, reducing the sidelobe-induced is the mainly focus in our future work. The distance corresponding to each azimuth slice is [1.5,2.5]m, and the slant range resolution is calculated according to c/2B = 0.0214m, yielding a measurement matrix with dimensional of $281 \times (73 \times 46)$, reconstructions are all performed with SBL algorithm. Imaging results are given in Fig. 12(e-g), we can clearly see that all three scatterers in each azimuth slice are well preserved without artifacts. Fig. 11(h) is the front view is obtained by maximum projection of the 3-D image onto the *yz* plane, and polar coordinates in *z* axis is transformed to Cartesian coordinates.

(a)   (b)

(c)   (d)

(e)   (f)

(g)   (h)
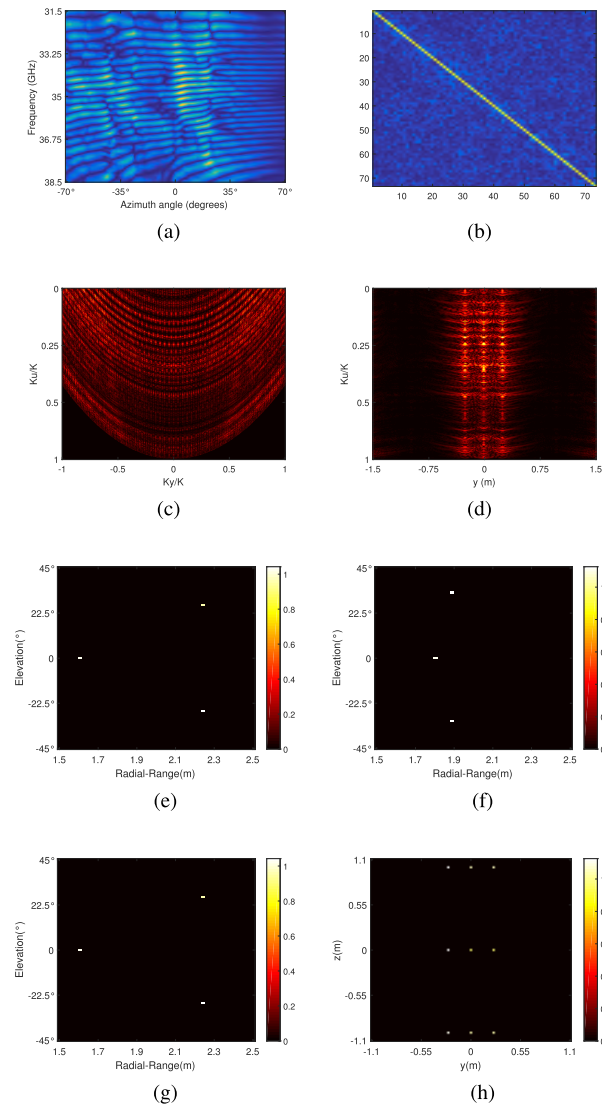
FIGURE 11. 3D imaging results using omega-K algorithm. (a) Magnitude distribution of the simulated radiation field pattern T. (b) Gram matrix. (c) Transformed signal $S(K_u, K_y)$. (d) Azimuth focusing results. (e) Slant range and elevation distribution corresponding to azimuth $y = 0.25\text{m}$. (f) Slant range and elevation distribution corresponding to azimuth $y = 0\text{m}$. (g) Slant range and elevation distribution corresponding to azimuth $y = -0.25\text{m}$. (h) Front view of image.

VII. CONCLUSIONS

Focusing on the peculiar conjunction of computation imaging and synthetic aperture radar technologies, in this paper, we mainly propose two different postprocessing algorithms to achieve fully 3D images of scene space. The crux of the processing relies on the decoupling of antenna movement dimension and the platform direction. By leveraging classical SAR processing algorithms, 3D imaging space is firstly partitioned into a number of cross range slices, the slant range and elevation distributions are then reconstructed by means of computational imaging techniques. In general, for the two algorithms discussed above, BP integral algorithm is more accurate but suffers from the low computation efficiency,

especially when comes to the imaging scene of large data sets. Meanwhile, omega-K is more efficient and no need for the prior information of ROI in imaging space. Future studies will mainly focus on the practical algorithm implementation in real-world imaging scenarios.

REFERENCES
[1] D. M. Sheen, D. L. McMakin, and T. E. Hall, "Three-dimensional millimeter-wave imaging for concealed weapon detection," *IEEE Trans. Microw. Theory Techn.*, vol. 49, no. 9, pp. 1581–1592, Sep. 2001.

[2] A. Shayei, Z. Kavehvash, and M. Shabany, "Improved-resolution millimeter-wave imaging through structured illumination," *Appl. Opt.*, vol. 56, no. 15, pp. 4454–4456, 2017.

[3] X. Zhuge and A. G. Yarovoy, "Three-dimensional near-field MIMO array imaging using range migration techniques," *IEEE Trans. Image Process.*, vol. 21, no. 6, pp. 3026–3033, Jun. 2012.

[4] E. J. Bond, X. Li, S. C. Hagness, and B. D. Van Veen, "Microwave imaging via space-time beamforming for early detection of breast cancer," *IEEE Trans. Antennas Propag.*, vol. 51, no. 8, pp. 1690–1705, Aug. 2003.

[5] S. Kharkovsky and R. Zoughi, "Microwave and millimeter wave nondestructive testing and evaluation—Overview and recent advances," *IEEE Instrum. Meas. Mag.*, vol. 10, no. 2, pp. 26–38, Apr. 2007.

[6] M. Dehmollaian and K. Sarabandi, "Refocusing through building walls using synthetic aperture radar," *IEEE Trans. Geosci. Remote Sens.*, vol. 46, no. 6, pp. 1589–1599, Jun. 2008.

[7] Q. Huang, L. Qu, B. Wu, and G. Fang, "UWB through-wall imaging based on compressive sensing," *IEEE Trans. Geosci. Remote Sens.*, vol. 48, no. 3, pp. 1408–1415, Mar. 2010.

[8] A. Zomet and S. K. Nayar, "Lensless imaging with a controllable aperture," in *Proc. IEEE Comput. Soc. Conf. Comput. Vis. Pattern Recognit. (CVPR)*, vol. 1, Jun. 2006, pp. 339–346.

[9] B. Sun et al., "3D computational imaging with single-pixel detectors," *Science*, vol. 340, pp. 844–847, May 2013.

[10] D. L. Marks, J. Gollub, and D. R. Smith, "Spatially resolving antenna arrays using frequency diversity," *J. Opt. Soc. Amer. A, Opt. Image Sci.*, vol. 33, no. 5, pp. 899–912, 2016.

[11] J. Hunt et al., "Metamaterial apertures for computational imaging," *Science*, vol. 339, no. 6117, pp. 310–313, Jan. 2013.

[12] G. Lipworth et al., "Metamaterial apertures for coherent computational imaging on the physical layer," *J. Opt. Soc. Amer. A, Opt. Image Sci.*, vol. 30, no. 8, pp. 1603–1612, 2013.

[13] J. Hunt et al., "Metamaterial microwave holographic imaging system," *J. Opt. Soc. Amer. A, Opt. Image Sci.*, vol. 31, no. 10, pp. 2109–2119, Oct. 2014.

[14] G. Lipworth et al., "Comprehensive simulation platform for a metamaterial imaging system," *Appl. Opt.*, vol. 54, no. 31, pp. 9343–9353, 2015.

[15] T. Sleasman, M. F. Imani, J. N. Gollub, and D. R. Smith, "Dynamic metamaterial aperture for microwave imaging," *Appl. Phys. Lett.*, vol. 107, no. 20, Nov. 2015, Art. no. 204104.

[16] T. Sleasman, M. F. Imani, J. N. Gollub, and D. R. Smith, "Microwave imaging using a disordered cavity with a dynamically tunable impedance surface," *Phys. Rev. Appl.*, vol. 6, no. 5, 2016, Art. no. 054019.

[17] O. Yurduseven, V. R. Gowda, J. N. Gollub, and D. R. Smith, "Printed aperiodic cavity for computational and microwave imaging," *IEEE Microw. Wireless Compon. Lett.*, vol. 26, no. 5, pp. 367–369, May 2016.

[18] T. Fromenteze et al., "Computational imaging using a mode-mixing cavity at microwave frequencies," *Appl. Phys. Lett.*, vol. 106, no. 19, 2015, Art. no. 194104.

[19] M. Alibakhshi-kenari et al., "Interaction between closely packed array antenna elements using meta-surface for applications such as MIMO systems and synthetic aperture radars," *Radio Sci.*, vol. 53, no. 11, pp. 1368–1381, Nov. 2018.

[20] M. Alibakhshi-kenari, M. Naser-Moghadasi, R. A. Sadeghzadeh, B. S. Virdee, and E. Limiti, "Periodic array of complementary artificial magnetic conductor metamaterials-based multiband antennas for broadband wireless transceivers," *IET Microw., Antennas Propag.*, vol. 10, no. 15, pp. 1682–1691, Dec. 2016.

[21] T. Sleasman *et al.*, "Experimental synthetic aperture radar with dynamic metasurfaces," *IEEE Trans. Antennas Propag.*, vol. 65, no. 12, pp. 6864–6877, Dec. 2017.

[22] C. M. Watts, A. P. Engel, D. R. Smith and M. S. Reynolds, "X-band SAR imaging with a liquid-crystal-based dynamic metasurface antenna," *J. Opt. Soc. Amer. B, Opt. Phys.*, vol. 34, no. 2, pp. 300–306, Feb. 2017.

[23] S. Devadithya, A. Pedross-Engel, C. M. Watts, N. I. Landy, T. Driscoll, and M. S. Reynolds, "GPU-accelerated enhanced resolution 3-D SAR imaging with dynamic metamaterial antennas," *IEEE Trans. Microw. Theory Techn.*, vol. 65, no. 12, pp. 5096–5103, Dec. 2017.

[24] L. Pulido-Mancera *et al.*, "Application of range migration algorithms to imaging with a dynamic metasurface antenna," *J. Opt. Soc. Amer. B, Opt. Phys.*, vol. 33, no. 10, pp. 2082–2092, Oct. 2016.

[25] A. V. Diebold, L. Pulido-Mancera, T. Sleasman, M. Boyarsky, M. F. Imani, and D. R. Smith, "Generalized range migration algorithm for synthetic aperture radar image reconstruction of metasurface antenna measurements," *J. Opt. Soc. Amer. B, Opt. Phys.*, vol. 34, no. 12, pp. 2610–2623, Dec. 2017.

[26] D. M. Sheen, D. L. McMakin, and T. E. Hall, "Cylindrical millimeter-wave imaging technique and applications," *Proc. SPIE*, vol. 6211, May 2006, Art. no. 62110A.

[27] D. R. Smith, O. Yurduseven, L. Pulido-Mancera, P. Bowen, and N. B. Kundtz "Analysis of a waveguide-fed metasurface antenna," *Phys. Rev. Appl.*, vol. 8, no. 5, 2017, Art. no. 054048.

[28] J. Hunt. *Metamaterials for Computational Imaging*. Durham, NC, USA: Duke Univ., 2013.

[29] Z. Wu, L. Zhang, H. liu, and N. Kou, "Range decoupling algorithm for accelerating metamaterial apertures-based computational imaging," *IEEE Sensors J.*, vol. 18, no. 9, pp. 3619–3631, May 2018.

[30] L. M. H. Ulander, H. Hellsten, and G. Stenstrom, "Synthetic-aperture radar processing using fast factorized back-projection," *IEEE Trans. Aerosp. Electron. Syst.*, vol. 39, no. 3, pp. 760–776, Jul. 2003.

[31] D. E. Wahl, D. A. Yocky, and C. V. Jakowatz, "An implementation of a fast backprojection image formation algorithm for spotlight-mode SAR," *Proc. SPIE*, vol. 6970, pp. 700H-9–700H-11, Apr. 2008.

[32] C. V. Jakowatz, D. E. Wahl, and D. Yocky, "Beamforming as a foundation for spotlight-mode SAR image formation by backprojection," *Proc. SPIE*, vol. 6970, Apr. 2008, Art. no. 69700Q.

[33] C. V. Jakowatz and D. E. Wahl, "Considerations for autofocus of spotlight-mode SAR imagery created using a beamforming algorithm," *Proc. SPIE*, vol. 7337, Apr. 2009, Art. no. 73370A.

[34] D. P. Wipf and B. D. Rao, "Sparse Bayesian learning for basis selection," *IEEE Trans. Signal Process.*, vol. 52, no. 8, pp. 2153–2164, Aug. 2004.

ZHENHUA WU was born in Anhui, China, in 1993. He received the B.S. degree in electronic engineering from Xidian University, Xi'an, China, in 2014, where he is currently pursuing the Ph.D. degree in signal processing with the National Laboratory of Radar Signal Processing. His research interests include radar imaging and sparse signal processing.

LEI ZHANG was born in Zhejiang, China, in 1984. He received the Ph.D. degree, in 2011. He was an Associate Professor with the National Laboratory of Radar Signal Processing, Xidian University, from 2012 to 2019. He is currently an Associate Professor with the School of Electronics and Communication Engineering, Sun Yat-sen University. His major research interests include radar imaging (SAR/ISAR) and motion compensation.

HONGWEI LIU (M'04) received the M.S. and Ph.D. degrees in electronic engineering from Xidian University, Xi'an, China, in 1995 and 1999, respectively. He was with the National Laboratory of Radar Signal Processing, Xidian University. From 2001 to 2002, he was a Visiting Scholar with the Department of Electrical and Computer Engineering, Duke University, Durham, NC, USA. He is currently a Professor with the National Laboratory of Radar Signal Processing, Xidian University. His research interests include radar automatic target recognition, radar signal processing, and adaptive signal processing.

• • •